Journal of Radiological Protection

Official journal of the Society for Radiological Protection

Patient radiation dose from x-ray guided endovascular aneurysm repair: A Monte Carlo approach using voxel phantoms and detailed exposure information

To cite this article before publication: Richard W Harbron *et al* 2020 *J. Radiol. Prot.* in press https://doi.org/10.1088/1361-6498/ab944e

Patient radiation dose from x-ray guided endovascular aneurysm repair: A Monte Carlo approach using voxel phantoms and detailed exposure information

Richard W Harbron[1, 2*], Mohamed Abdelhalim[3], Elizabeth A Ainsbury[3,4], Jonathan S Eakins[3,4], Azeem Alam[3], Choonsik Lee[5], Bijan Modarai[3]

[1]Institute of Population Health Sciences, Newcastle University, Royal Victoria Infirmary, Queen Victoria Road, Newcastle-upon-Tyne, NE1 4LP, UK.

[2]NIHR Health Protection Research Unit in Chemical and Radiation Threats and Hazards, Newcastle University, UK.

[3]Academic Department of Vascular Surgery, School of Cardiovascular Medicine and Sciences, King's College London, BHF Centre of Excellence at Guy's and St Thomas' NHS Foundation Trust, London, United Kingdom

[4]Public Health England Centre for Radiation, Chemical and Environmental Threats and Hazards, Chilton, Oxfordshire, UK.

[5] Division of Cancer Epidemiology and Genetics, National Cancer Institute, National Institutes of Health, Bethesda, Maryland, USA

*Corresponding author:

Richard W Harbron
4th Floor, Sir James Spence Institute
Royal Victoria Infirmary
Queen Victoria Road
Newcastle-upon-Tyne
NE1 4LP, UK
Richard.harbron@ncl.ac.uk
0191 282 1354

Abstract:

Endovascular aneurysm repair (EVAR) is a well-established minimally invasive technique that relies on x-ray guidance to introduce a stent through the femoral artery and manipulate it into place. The aim of this study was to estimate patient organ and effective doses from EVAR procedures using anatomically realistic computational phantoms and detailed exposure information from radiation dose structured reports (RDSR). Methods: Lookup tables of conversion factors relating kerma area product (P_{KA}) to organ doses for 49 different beam angles were produced using Monte Carlo simulations (MCNPX2.7) with ICRP adult male and female voxel phantoms for EVAR procedures of varying complexity (infrarenal, fenestrated/branched and thoracic EVAR). Beam angle specific correction factors were calculated to adjust doses according to x-ray energy. A MATLAB function was written to find the appropriate conversion factor in the lookup table for each exposure described in the RDSR, perform energy corrections, and multiply by the respective exposure P_{KA}. Using this approach, organ doses were estimated for 183 EVAR procedures in which RDSRs were available. A number of simplified dose estimation methodologies were also investigated for situations in which RDSR data are not available. Results: Mean estimated bone marrow doses were 57 (range: 2-247), 86 (2-328) and 54 (8-250) mGy for infra-renal, fenestrated/branched and thoracic EVAR respectively. Respective effective doses were 27 (1-208), 54 (1-180) and 37 (5-167) mSv. Dose estimates using non-individualised, average conversion factors, along with those produced using the alternative Monte Carlo code PCXMC, yielded reasonably similar results overall, though variation for individual procedures could exceed 100% for some organs. In conclusion, radiation doses from x-ray guided endovascular aneurysm repairs are potentially high, though this must be placed in the context of the life sparing nature and high success rate for this procedure.

Introduction:

Aortic aneurysms occur when a section of the blood vessel wall weakens, allowing a balloon-like bulge to develop. Rupture of aortic aneurysms usually result in catastrophic haemorrhage and death (Albert Einstein was a notable sufferer). Even if the patient makes it alive to hospital, emergency surgery for a ruptured aneurysm can have a mortality as high as 70% (1). The preferred management for known aneurysms, once they reach a threshold size, is to carry out elective repair to circumvent the risk of rupture. Endovascular aortic aneurysm repair (EVAR) is a minimally invasive technique that offers the chance to reline the aorta from within, using a stent graft, thus excluding the aneurysm from the circulation. The procedure relies on the use of x-ray guidance to introduce and manipulate the stent graft within the aorta. As experience with this technique has increased, so has the complexity of repairs performed, some involving the use of multiple stent components during procedures lasting several hours. This has recently focused attention on the possible deleterious effects of the consequent radiation exposure, including studies that have suggested an increased risk of malignancy in patients after EVAR, but this evidence is by no means conclusive (2, 3).

Due to the procedural complexity, and the thickness and density of the abdominal region, EVAR has the potential to deliver particularly high radiation doses. Air kerma at the entrance skin surface may reach several gray (Gy), while kerma area product (P_{KA}) frequently exceeds several hundred Gy cm^2 (4-6). Aside from these simple dose indicators, published estimates of patient dose have been almost entirely restricted to effective dose. Figures are typically in the range 10-100 mSv (4, 5, 7-11), though figures of up to 1000 mSv have been reported (4). All estimates of effective dose have been obtained using the Monte Carlo code PCXMC (STUK, Helsinki, Finland) (12). The deficiencies of the modified Oak Ridge National Laboratories (ORNL) phantom models (13) used in PCXMC are well known (e.g. (14)). Organ shapes are very simplistic and there are no separate male and female phantoms. Furthermore, although EVAR procedures involve a range of beam angles, no evaluation of the impact of beam angle on organ doses appears to have been performed. Information on organ doses from EVAR is currently very limited.

We sought to address these limitations by using a Monte Carlo (MC) approach to estimate organ doses with realistic phantom models and incorporating detailed information on beam angles and x-ray beam spectra. The study utilised a 'lookup table' methodology in which a library of conversion factors relating input dose (P_{KA}) to various organ doses is produced for a wide range of conditions. Doses can then be estimated without needing to perform new simulations by matching exposure conditions to the appropriate conversion factor.

Procedure description:

The term 'EVAR' is used to refer to a group of procedures of varying complexity used to treat aneurysms of the aorta. The simplest of these is the infra-renal EVAR (IEVAR), which is used when the aneurysm affects the lower portion of the aorta below the renal arteries (supplying the kidneys). IEVAR was the first of these procedures to be developed and is the least time consuming, generally leading to the least radiation exposure. Aneurysms involving the descending thoracic aorta, above the coeliac trunk, are treated with a thoracic EVAR (TEVAR) (15). These are difficult procedures, associated with higher mortality and risk of stroke and spinal cord ischaemia (16). The central portion of the aorta, in the upper abdomen, gives rise to the coeliac trunk, the superior mesenteric artery and the renal arteries, vessels that supply much of the vital intra-abdominal organs. Unlike stent grafts used for IEVAR and TEVAR, devices used in this region are especially designed to allow the aforementioned vessels to be incorporated in the repair, making repair of aneurysms in this aortic much more complex. Fenestrated EVAR (FEVAR) describes the situation where the fabric of the stent graft covers the aorta adjacent to one or more of these arteries (target vessels), but perfusion is maintained through accurately placed windows (fenestrations) in the fabric directly in front of the orifice of the target vessel (15). Branched EVAR (BEVAR) is when these vital arteries arise from the dilated aneurysmal segment of the aorta and therefore there is a gap between the stent graft and the aortic wall with its branches (15). This gap needs to be bridged with further stents into the target vessels in order to maintain perfusion to the vital organs. Due to the increased complexity, FEVAR and BEVAR are more time-consuming procedures involving more fluoroscopy time and digital

subtraction angiography (DSA) runs than IEVAR and TEVAR. Therefore, they generally involve more radiation exposure to the patient (4, 17).

Methods:

Monte Carlo simulations were performed using the general purpose radiation transport code MCNPX2.7 (Los Alamos National Laboratory, New Mexico, USA) (18). Detailed specifications are provided in Appendix 1. We used the reference adult male and female voxel phantoms published by the International Commission on Radiological Protection (ICRP) (19). Both phantoms were created from cross sectional images of individuals who had undergone whole body CT scanning during treatment for leukaemia. Neither patient had any structural abnormality. The male phantom is based on a 38-year-old individual of height 178 cm and mass 70 kg. The female phantom is based on a 43-year-old, of height 167 cm and mass 59 kg (19). A detailed specification of these phantoms is provided in Appendix 2. Both phantoms had their arms removed, to prevent any shielding effect for laterally orientated projections, and were placed on a table of 1 cm thickness, made of carbon (density = 1.4 g cm^{-3}).

An isocentric coordinate system was developed to calculate the source position, source direction vector and collimator window position and orientation for any specified beam angle, centring point and field size. The beam was collimated by means of two concentric spherical shells, of radius 64.5 and 64.6 cm, surrounding the patient. The phantom's legs are partially outside the collimator shells in the model, although the dose to the excluded regions is close to zero. The region between the spheres was assigned an MCNP 'importance' of zero, meaning that the histories of any particles entering this region were terminated. The source was placed outside the collimator spheres at a distance of 75 cm from the isocentre. This distance was representative of clinical exposure conditions. An output window, which also served as a P_{KA} meter, was placed to allow x-rays to pass through the collimator spheres and irradiate the required region (Figure 1). The size of the output window was adjusted to irradiate the region of interest, depending on the specific type of EVAR:

- IEVAR: Between the renal arteries and just below the bifurcation of the aorta (Figure 2)

- FEVAR/BEVAR: the whole abdominal aorta, from the diaphragm to just below the bifurcation
- TEVAR: whole thoracic aorta, from the lung apices to the diaphragm

The source was forward biased, along its direction vector, to expose a region slightly larger than the collimator window.

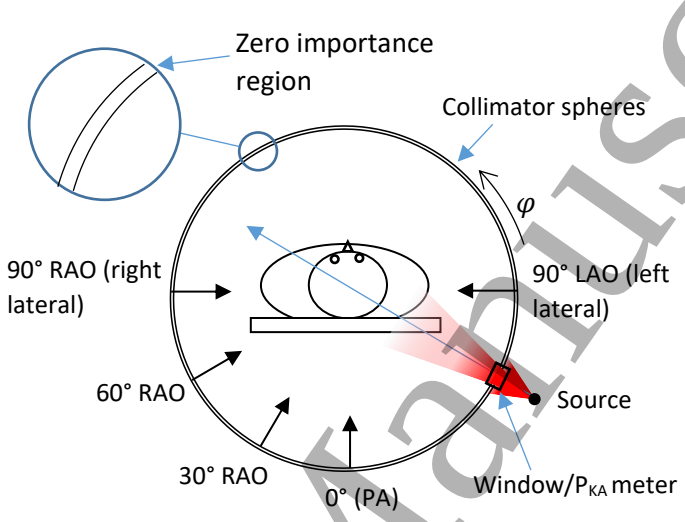

Figure 1: Irradiation geometry looking along patient long axis from head to foot. Note: not drawn to scale!

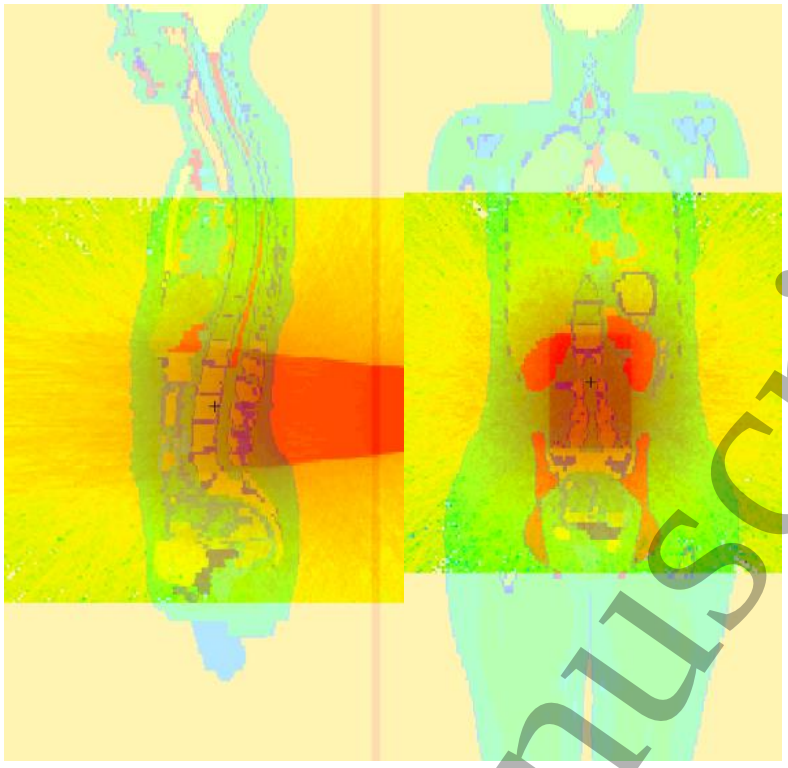

Figure 2: Mid-sagittal and coronal view of female ICRP phantom with superimposed photon mesh tally showing exposed field for infra-renal EVAR.

Only photons were transported in the MCNP simulations, meaning secondary electrons were not tracked and all energy was assumed to be deposited locally. This greatly improved the computational efficiency of the calculations. Given the relatively low photon energies used in simulations (up to 120 keV), the range of secondary electrons would seldom exceed 100 μm in water (20), thus this approximation can be considered reasonable. Doses were calculated by MCNPX for all organs using the f6 tally with the equivalence between dose and kerma assumed explicitly from the assumption of secondary charged particle equilibrium. The conversion factor (CF) relating P_{KA} to organ dose D ($CF_{P_{KA}\to D}$), in mGy/Gy cm^2 between absorbed dose to each organ and P_{KA} was calculated as:

$$CF_{P_{KA}\to D} = \frac{1000 \times T_O}{T_W \times A_W}$$

Where A_W is the area of the collimator window (in cm^2) normal to the beam central axis, T_O is the dose tally (in MeV/g) to the organ and T_W is the dose tally, in air, to the window cell. For each simulation, 10^7 photons were tracked. This resulted in MC simulation statistical uncertainties of well

below 5% for all in-field and beam bordering organs considered in this study and for all organs making a meaningful contribution to effective dose. Non-statistical, or systematic uncertainties in the modelling are harder to estimate, though it is noted that MCNP is very well benchmarked for the types of exposure of current interest (18).

Active bone marrow dose was calculated by scoring absorbed dose within the spongiosa regions in different bone sites, weighted by the bone site-specific distribution of active bone marrow (21). ICRP Publication 116 (22) notes that this approach provides reasonable estimation of the values calculated from dose response functions.

Monte Carlo simulations were used to create a lookup table of $CF_{P_{KA}\rightarrow D}$ conversion factors for 49 different beam angles, as described below. Different lookup tables were created for each of 17 organs and tissues. The x-ray beam may be angulated around the patient in the axial plane, denoted φ, and in the cranio-caudal direction (head to foot), denoted ϑ (Figures 1, 3). Simulations were performed in the range $CRA45° \leq \vartheta \leq CAU45°$ in 15° intervals and $LAO90° \leq \varphi \leq RAO90°$ in 30° intervals (CRA/CAU = cranial/caudal, RAO/LAO = right/left anterior oblique). This process was performed for both male and female phantoms, and for seven different x-ray spectra, calculated using Spekcalc (23) (Table 1). These spectra were based on a range of combinations of tube potential and added copper filtration typical of clinical practice, as determined from a sample of radiation dose structured reports (discussed below). For each of the 49 different beam angles, a 2nd degree polynomial was fitted to the relationship between half value layer (HVL), also calculated using Spekcalc, and organ dose, relative to a HVL of 7.08 mm (representing 80 kV and 0.4 mm Cu). This choice of 'reference' HVL was arbitrary and makes no difference.

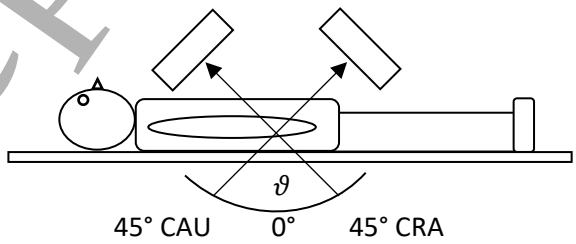

Figure 3: Irradiation geometry for cranio-caudal beam angulation. CRA = cranial angulation, CAU = caudal angulation

Table 1: Beam spectra used in simulations, defined by tube potential and added copper (Cu) and aluminium (Al) filtration. HVL = half value layer

Spectrum	Peak tube potential (kVp)	Cu (mm)	Al (mm)	1st HVL (mm Al)
1	50	0.1	3.5	2.96
2	60	0.4	3.5	5.3
3	80	0.1	3.5	4.75
4	80	0.4	3.5	7.08
5	100	0.1	3.5	5.87
6	100	0.4	3.5	8.46
7	120	0.4	3.5	9.49

A function was written in MATLAB (vR2018a, Mathworks, Natick, New Hampshire, USA) to pick the appropriate conversion factor from the lookup tables according to specified beam angle (combination of ϑ and φ) and patient sex. For beam angles in between the simulated intervals, $CF_{P_{KA}\to D}$ was calculated by linear interpolation. Initially, doses were calculated for the reference HVL of 7.08 mm, then adjusted to the specified HVL using the appropriate energy correction polynomial described above. Finally, the estimated dose for an exposure was calculated by multiplying the energy adjusted $CF_{P_{KA}\to D}$ by the respective exposure P_{KA}.

Dose estimates for clinical procedures:

The lookup-table-based MATLAB function described above was used to estimate organ doses for a sample of clinical procedures. Fully anonymized radiation dose structured reports (RDSRs) were obtained for 183 EVAR procedures (81 IEVAR, 66 FEVAR/BEVAR and 36 TEVAR) performed using a Philips Allura Xper FD20 system (Philips Healthcare, Eindhoven, the Netherlands) between 2017 and 2019. These RDSRs give information on all x-ray exposures (both fluoroscopy and digital acquisitions), including beam angle, tube potential (kVp), added filtration and P_{KA}. For each exposure, the combination of kVp and added Cu filtration was converted to HVL in mm Al. The total examination dose for each organ was calculated as the sum of doses for all exposures described in the RDSR for that examination.

For the IEVAR procedures, we also investigated a number of simplified approaches to estimating doses for cases where RDSRs are not available. This allowed the potential errors to be evaluated that result from dose estimation using limited information, *e.g.* total examination P_{KA} only. Firstly, organ doses for each procedure were divided by the total procedural P_{KA}, giving a single $CF_{P_{KA}\rightarrow D}$ conversion factor, taking into account all the various beam angles and x-ray spectra used throughout the procedure. The average 'whole procedure' conversion factor for all 81 IEVAR procedures was then calculated for each organ and used to estimate doses for individual procedures using total P_{KA}. For the second approach, doses were estimated with 100% of P_{KA} delivered in the PA projection, as is typically assumed in similar studies.

As a further comparison, doses were also estimated using the alternative Monte Carlo code PCXMC (V2.0). PCXMC is well-suited to utilising RDSRs (e.g. (24, 25)) as data can be inputted into the 'Autocalc' Excel spreadsheet with minimal preparation. Separate simulations were performed for each exposure listed in the RDSR, taking into account beam angle, kVp and filtration. Simulations were performed with 50,000 photons, which was sufficient to keep simulation MC uncertainties well below 5% for organs of interest. Field size and centring point were kept constant for each EVAR type. The modified ORNL phantom models used in PCXMC (13) do not feature an aorta, let alone the bifurcation or arch of this vessel, meaning defining an appropriate exposure region was challenging.

Results:

Estimated organ doses are shown in Tables 2-4 for IEVAR, FEVAR/BEVAR and TEVAR respectively. These organ doses are based on median P_{KA} values of 75 Gy cm^2 (interquartile range: 48-148) for IEVAR, 119 Gy cm^2 (85, 209) for FEVAR/BEVAR and 110 Gy cm^2 (50-165) for TEVAR. Tables 6-8 show average $CF_{P_{KA}\rightarrow D}$ conversion factors for each procedure type. For the abdominal aorta EVAR procedures (IEVAR, BEVAR, FEVAR), doses were highest for the kidneys, pancreas, colon and small intestine. Estimated kidney doses exceeded 200 mGy for 19% of infra-renal, 44% of FEVAR/BEVAR procedures. Active bone marrow (ABM) dose was also high, with mean doses exceeding 50 mGy for all procedure types. This is primarily due to the contribution of

marrow in the spine. Consequently, ABM dose tended to be higher for PA-orientated projections (Figure 4). Conversely, colon and kidney doses were higher for more laterally orientated projections.

*Table 2: Estimated organ doses (in mGy) for 81 infra-renal endovascular aneurysm repairs. STD = standard deviation, IQR = interquartile range, * females only*

Organ	Estimated dose (mGy)		
	Mean [STD]	Median [IQR]	Range
Thyroid	0 [0]	0 [0, 1]	0 - 2
Oesophagus	5 [5]	3 [2, 6]	0 - 20
Lungs	4 [4]	2 [2, 5]	0 - 16
Breasts*	1 [2]	1 [0, 1]	0 - 5
Heart	5 [6]	3 [2, 6]	0 - 28
Stomach	30 [46]	16 [9, 29]	1 - 279
Liver	28 [42]	14 [8, 34]	0 - 329
Gall bladder	52 [74]	28 [16, 62]	1 - 557
Adrenals	69 [68]	44 [25, 96]	1 - 343
Spleen	25 [33]	14 [8, 24]	1 - 151
Pancreas	91 [103]	54 [33, 112]	2 - 473
Kidneys	150 [184]	83 [46, 168]	4 - 983
Small Intestine	77 [131]	37 [20, 77]	2 - 919
Colon	73 [159]	26 [14, 61]	1 - 1095
Urinary bladder	6 [7]	4 [2, 7]	0 - 32
Active bone marrow	57 [55]	36 [24, 71]	2 - 247

*Table 3: Estimated organ doses (in mGy) for 66 fenestrated or branched endovascular aneurysm repairs. STD = standard deviation, IQR = interquartile range, * females only*

Organ	Estimated dose (mGy)		
	Mean [STD]	Median [IQR]	Range
Thyroid	2 [1]	1 [1, 2]	0 - 6
Oesophagus	29 [21]	23 [14, 41]	1 - 108
Lungs	19 [13]	15 [10, 25]	0 - 65
Breasts*	5 [4]	4 [3, 8]	1 - 12
Heart	26 [19]	21 [14, 34]	1 - 88
Stomach	95 [76]	80 [41, 113]	2 - 349
Liver	96 [85]	70 [38, 112]	1 - 364
Gall bladder	105 [89]	83 [46, 126]	2 - 398
Adrenals	252 [188]	183 [134, 340]	5 - 959
Spleen	185 [182]	138 [67, 245]	3 - 1064
Pancreas	139 [105]	101 [69, 169]	3 - 520
Kidneys	248 [201]	176 [125, 315]	3 - 963
Small Intestine	91 [70]	72 [43, 112]	2 - 356
Colon	87 [75]	65 [40, 108]	1 - 338
Urinary bladder	5 [4]	4 [3, 6]	0 - 21
Active bone marrow	86 [63]	64 [46, 115]	2 - 328

*Table 4: Estimated organ doses (in mGy) for 36 thoracic endovascular aneurysm repairs. STD = standard deviation, IQR = interquartile range, * females only*

Organ	Estimated dose (mGy)		
	Mean [STD]	Median [IQR]	Range
Thyroid	22 [22]	16 [8, 25]	4 - 100
Oesophagus	103 [97]	86 [38, 118]	17 - 432
Lungs	123 [124]	94 [43, 141]	14 - 576
Breasts*	18 [17]	13 [8, 21]	4 - 65
Heart	114 [110]	84 [37, 141]	17 - 469
Stomach	24 [25]	18 [9, 26]	4 - 124
Liver	27 [30]	18 [11, 30]	2 - 151
Gall bladder	10 [10]	7 [3, 11]	1 - 49
Adrenals	19 [20]	15 [7, 20]	3 - 101
Spleen	45 [49]	29 [14, 49]	6 - 220
Pancreas	8 [9]	6 [3, 10]	1 - 46
Kidneys	9 [9]	6 [3, 10]	1 - 46
Small Intestine	2 [2]	2 [1, 3]	0 - 12
Colon	3 [3]	1 [1, 3]	0 - 17
Urinary bladder	0 [0]	0 [0, 0]	0 - 1
Active bone marrow	54 [54]	40 [21, 63]	8 - 250

Effective dose could not be estimated directly as we did not calculate separate MCNP tallies for bone surfaces and lymph nodes. Using PCXMC, we determined that the inclusion of these two tissues increased effective dose by approximately 3%, relative to effective dose calculated without bone or lymph nodes. We were then able to estimate effective dose by multiplying the figures obtained without the contribution of bones and lymph nodes by a factor of 1.03. Using this approach, the mean estimated effective doses for IEVAR, FEVAR/BEVAR and TEVAR procedures were 27, 54 and 37 mSv, respectively. Note that these 'effective doses' are sex-specific, rather than sex-averaged: although therefore not true effective dose, presentation of the data in this way is considered more insightful for the present purposes as a means of quantifying overall whole body exposures for the male and female separately. Of course, the ICRP advise against the use of true effective dose (26) for personalized dosimetry in any case. For abdominal region EVAR, effective dose was dominated by contributions from the colon, bone marrow, stomach and the 'remainder' category (including kidneys, gall bladder and small intestine).

Table 5: Average $CF_{P_{KA}\rightarrow D}$ conversion factors for organs (mGy/Gycm^2) and effective dose (mSv/Gycm^2) for infra-renal EVAR. Note: effective dose is sex-specific.

	Male		Female	
Organ	**Mean**	**Range**	**Mean**	**Range**
Thyroid	0.00	[0-0.01]	0.00	[0-0.01]
Oesophagus	0.04	[0.03-0.08]	0.03	[0.03-0.04]
Lungs	0.03	[0.02-0.06]	0.04	[0.03-0.05]
Breasts	-	-	0.01	[0.01-0.01]
Heart	0.04	[0.03-0.07]	0.04	[0.03-0.05]
Stomach	0.20	[0.14-0.59]	0.41	[0.27-0.89]
Liver	0.19	[0.11-0.68]	0.35	[0.19-0.69]
Gall bladder	0.37	[0.23-1.16]	0.65	[0.49-0.87]
Adrenals	0.58	[0.32-1.35]	0.79	[0.41-1.30]
Spleen	0.19	[0.05-0.52]	0.29	[0.17-0.62]
Pancreas	0.71	[0.57-0.95]	1.01	[0.86-1.40]
Kidneys	1.12	[0.74-2.04]	1.69	[1.24-2.29]
Small Intestine	0.55	[0.36-1.94]	0.62	[0.46-1.29]
Colon	0.44	[0.23-2.31]	0.57	[0.39-1.03]
Urinary bladder	0.05	[0.04-0.09]	0.04	[0.04-0.06]
Bone marrow	0.49	[0.33-0.66]	0.59	[0.49-0.67]
Effective dose	0.20	[0.14-0.44]	0.28	[0.21-0.38]

Table 6: Average $CF_{P_{KA}\rightarrow D}$ conversion factors for organs (mGy/Gycm^2) and effective dose (mSv/Gycm^2) for fenestrated/branched EVAR. Note: effective dose is sex-specific.

	Male		Female	
Organ	**Mean**	**Range**	**Mean**	**Range**
Thyroid	0.01	[0.01-0.01]	0.01	[0.01-0.02]
Oesophagus	0.18	[0.13-0.23]	0.21	[0.14-0.28]
Lungs	0.11	[0.07-0.14]	0.19	[0.15-0.25]
Breasts	0.03	[0.02-0.05]	0.05	[0.04-0.06]
Heart	0.16	[0.11-0.23]	0.21	[0.12-0.37]
Stomach	0.56	[0.30-0.99]	0.87	[0.31-1.98]
Liver	0.51	[0.23-1.07]	1.05	[0.69-1.56]
Gall bladder	0.57	[0.29-1.15]	1.06	[0.94-1.28]
Adrenals	1.52	[1.12-1.96]	1.83	[1.64-2.10]
Spleen	1.09	[0.29-3.15]	1.37	[0.31-4.52]
Pancreas	0.83	[0.55-1.07]	1.05	[0.73-1.44]
Kidneys	1.44	[0.87-2.14]	1.81	[1.35-2.96]
Small Intestine	0.57	[0.35-1.04]	0.54	[0.29-1.00]
Colon	0.55	[0.21-1.15]	0.46	[0.31-0.61]
Urinary bladder	0.03	[0.02-0.07]	0.03	[0.02-0.03]
Bone marrow	0.52	[0.39-0.69]	0.63	[0.51-0.71]
Effective dose	0.32	[0.21-0.47]	0.42	[0.3-0.64]

Table 7: Average $CF_{P_{KA}\to D}$ conversion factors for organs (mGy/Gycm²) and effective dose (mSv/Gycm²) for thoracic EVAR. Note: effective dose is sex-specific.

	Male		Female	
Organ	**Mean**	**Range**	**Mean**	**Range**
Thyroid	0.15	[0.09-0.21]	0.21	[0.16-0.24]
Oesophagus	0.65	[0.44-0.98]	1.19	[0.74-1.57]
Lungs	0.71	[0.59-0.89]	1.48	[1.00-1.99]
Breasts	-	-	0.22	[0.12-0.30]
Heart	0.67	[0.42-0.98]	1.47	[0.68-2.13]
Stomach	0.16	[0.07-0.24]	0.24	[0.09-0.38]
Liver	0.17	[0.10-0.30]	0.26	[0.19-0.42]
Gall bladder	0.06	[0.04-0.09]	0.10	[0.07-0.13]
Adrenals	0.14	[0.09-0.25]	0.16	[0.09-0.21]
Spleen	0.31	[0.09-0.63]	0.44	[0.13-0.75]
Pancreas	0.06	[0.04-0.09]	0.06	[0.03-0.08]
Kidneys	0.06	[0.04-0.11]	0.07	[0.04-0.10]
Small Intestine	0.02	[0.01-0.02]	0.02	[0.01-0.03]
Colon	0.02	[0.01-0.03]	0.01	[0.01-0.01]
Urinary bladder	0	[0-0]	0	[0-0]
Bone marrow	0.35	[0.28-0.53]	0.53	[0.46-0.63]
Effective dose	0.23	[0.18-0.29]	0.42	[0.29-0.53]

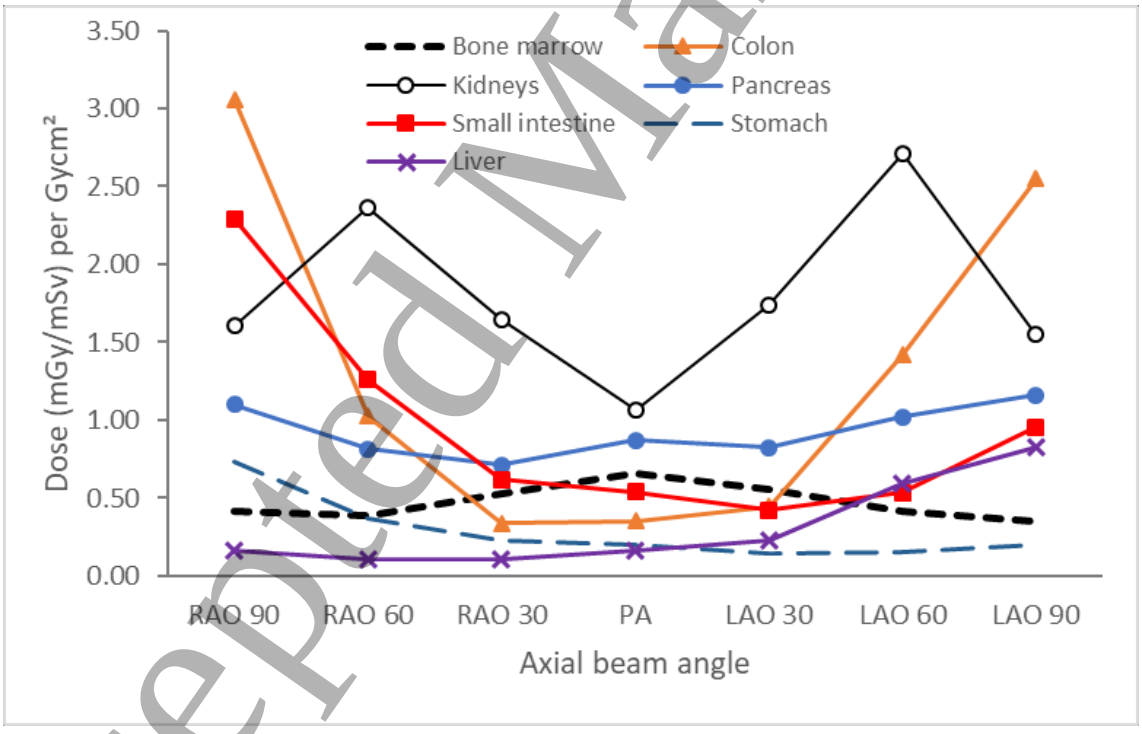

Figure 4: Variation in organ dose per unit P_{KA} with beam angle for infra-renal EVAR (cranio-caudal angle fixed at 0°). Figures calculated using the male ICRP phantom with a beam spectrum defined at 80 kV with 0.4 mm Cu filtration.

As a sensitivity analysis, simulations for the PA FEVAR/BEVAR field were repeated with a range of different field sizes and centring points. The 'high', 'mid' and 'low' fields were 40% shorter, in the head-foot direction, than the standard field and centred on the upper, middle and lower abdomen respectively. The 'narrow' field was the same length as the standard field but 23% narrower. The doses for these fields, relative to the standard field are shown in Figure 5. Doses for the narrow field were generally lower than for the standard field. The exception was for active bone marrow, which is primarily found in the spine in this region (thus receives a higher dose per unit P_{KA} for smaller field size). Otherwise, ABM dose was reasonably invariant to any of the other changes. Variation in organ doses with centring point was consistent with organ locations, e.g. for the 'high' field, stomach dose was greater but bladder dose was much lower.

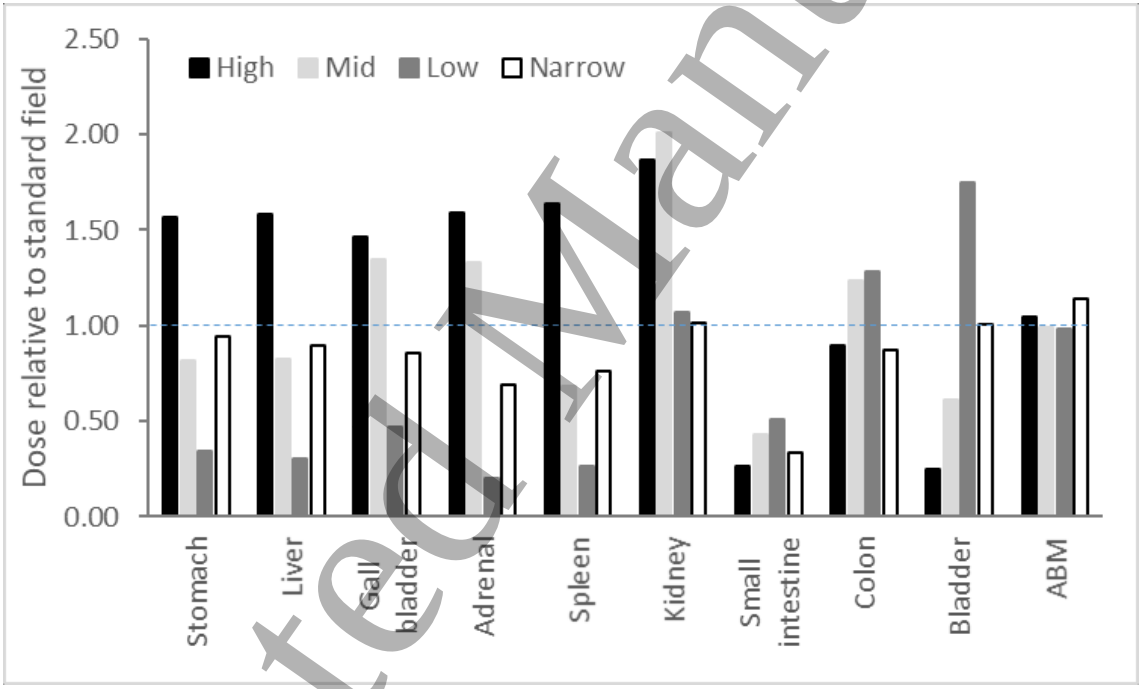

Figure 5: Impact of various changes to field size, relative to the 'standard' field, for fenestrated EVAR. ABM = active bone marrow. A relative dose greater than 1.0 implies doses are higher compared to the standard field.

Mean (sex averaged) effective doses calculated using PCXMC were 27, 44 and 33 mSv for IEVAR, FEVAR/BEVAR and TEVAR respectively, compared to 27, 54 and 37 mSv using the MCNP approach. The fairly large discrepancy for FEVAR/BEVAR appeared to be due to the impact of doses to the stomach, liver and colon, which are all higher using the MCNP approach. Figures 6-8 show the

relative difference in organ doses between PCXMC and MCNP. For individual procedures, the difference in organ dose between approaches could be large, occasionally exceeding 100%, with respect to MCNP. Likewise, using 'whole procedure' conversion factors resulted in reasonably similar average doses but with a large variation in dose for individual procedures (Figure 9). A maximum difference of +279% for the spleen occurred for a procedure in which an unusually large proportion of imaging was in the LAO projection, where spleen dose is reasonably low. Using the mean conversion factor thus grossly overestimated spleen dose for this procedure. For most organs, dose per unit P_{KA} is higher in laterally orientated projections than for PA, while for bone marrow the reverse is true (Figure 4). Assuming all exposures were in the PA projection thus tended to result in an underestimation of doses by 5-15%, while bone marrow doses were overestimated by around 15% (Figure 10).

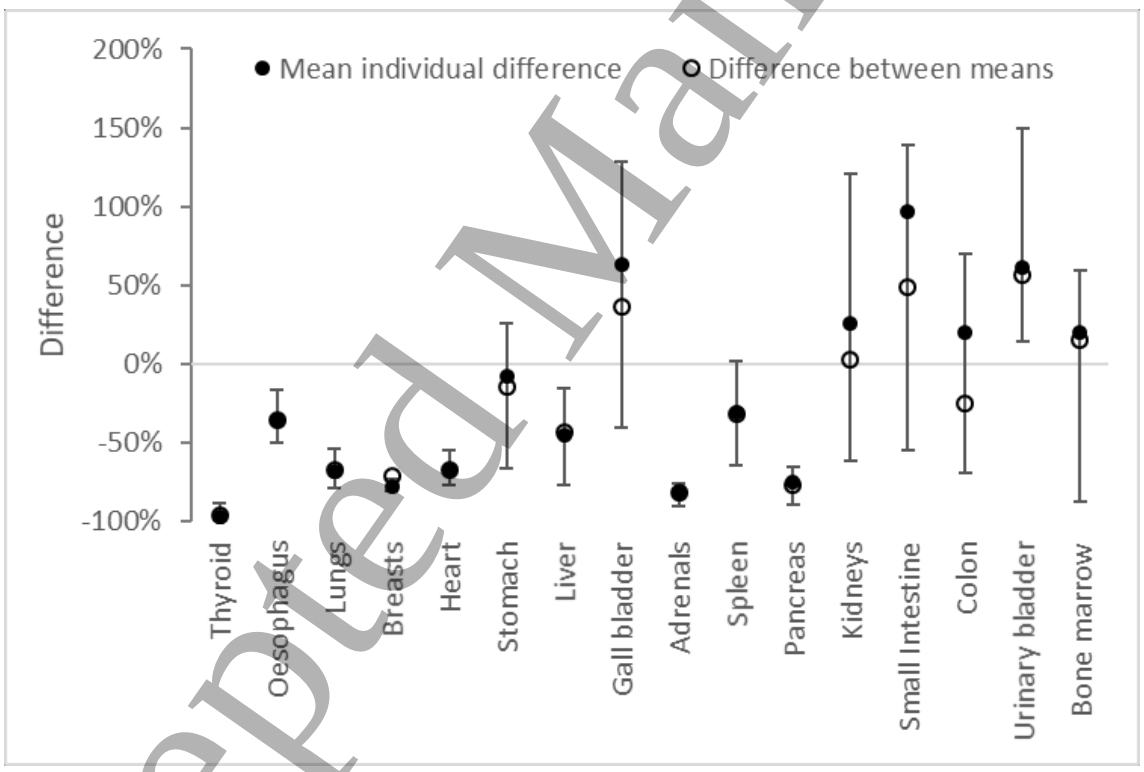

Figure 6: Percentage difference in estimated organ doses for infra-renal EVAR procedures calculated using MCNP (with ICRP voxel phantoms) and PCXMC (with modified ORNL phantoms), relative to the MCNP approach. A positive difference means that doses calculated using PCXMC were higher than MCNP. Vertical bars represent the range of differences. The 'mean individual difference' represents the mean % difference between organ doses for individual procedures

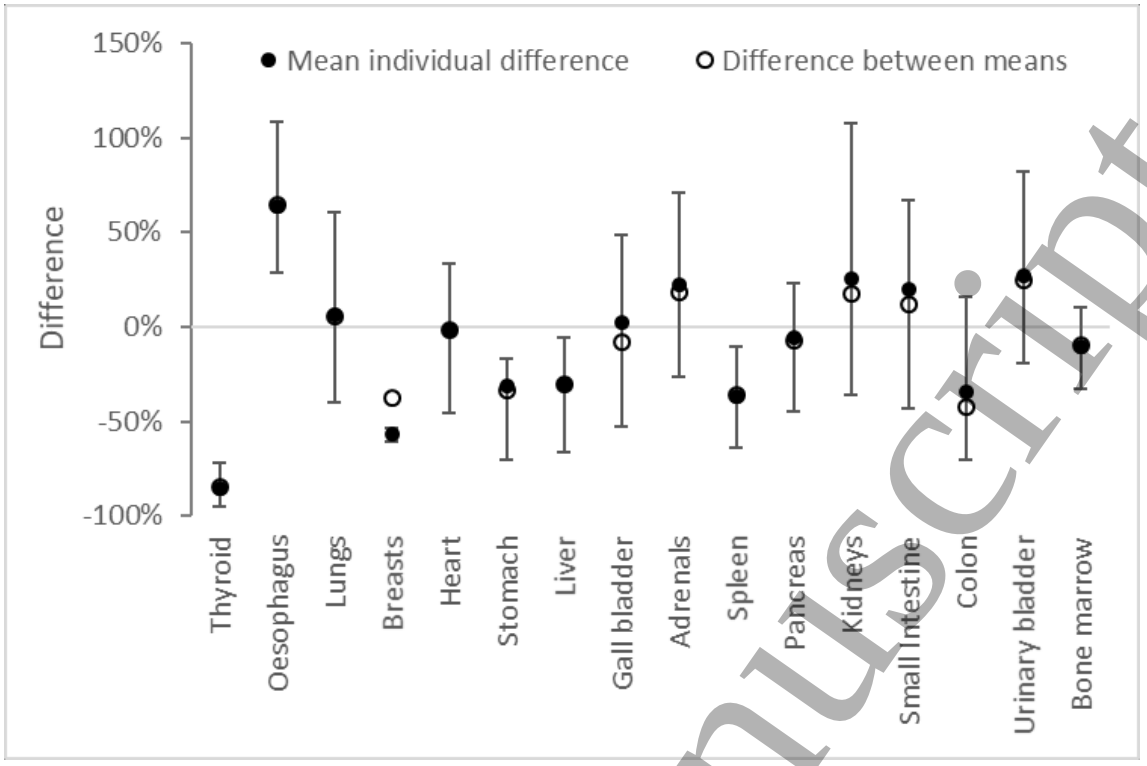

Figure 7: Percentage difference in estimated organ doses for fenestrated EVAR procedures calculated using MCNP with ICRP voxel phantoms and PCXMC with modified ORNL phantoms. A positive difference means that doses calculated using PCXMC were higher than MCNP. Vertical bars represent range of differences.

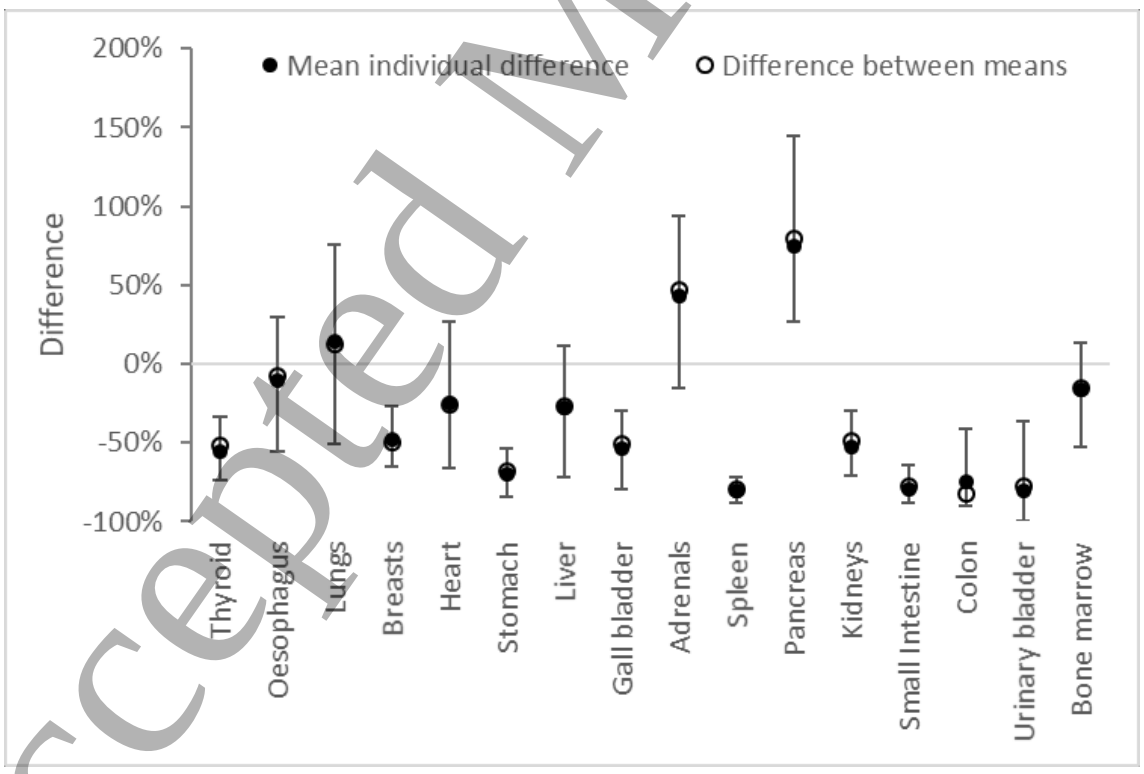

Figure 8: Percentage difference in estimated organ doses for thoracic EVAR procedures calculated using MCNP with ICRP voxel phantoms and PCXMC with modified ORNL phantoms. A positive difference means that doses calculated using PCXMC were higher than MCNP. Vertical bars represent range of differences.

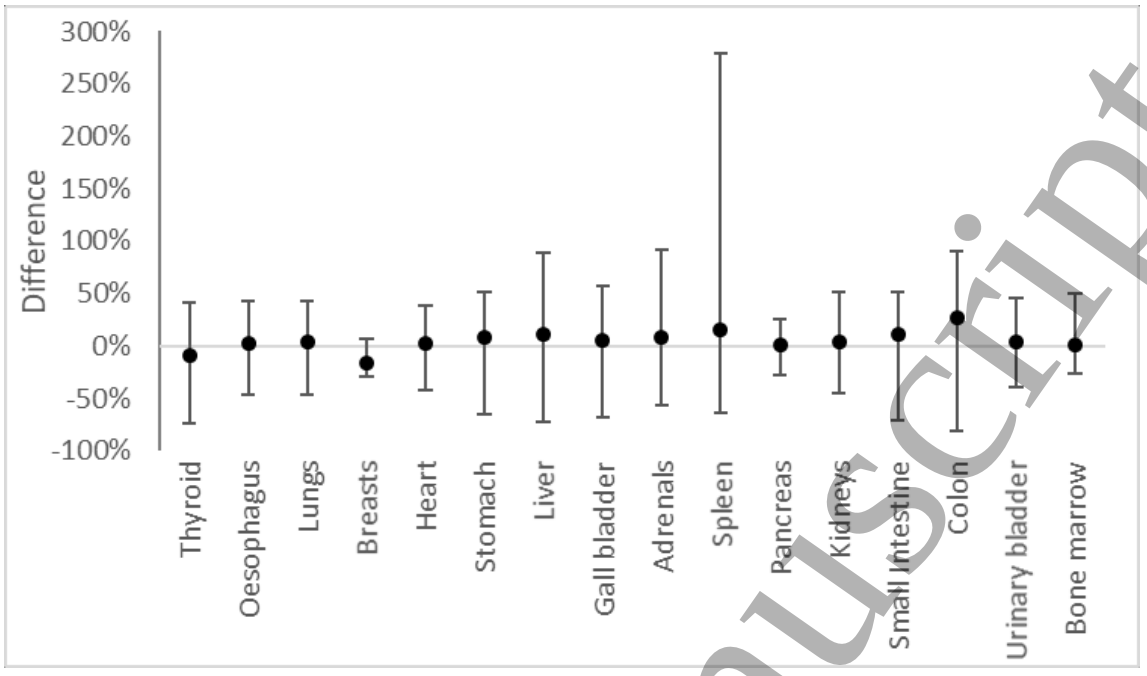

Figure 9: Mean difference in dose for infra-renal EVAR when using average conversion factors, relative to doses estimated using individual RDSR information. A positive difference means dose estimates were higher using average conversion factors. Vertical bars represent range of differences.

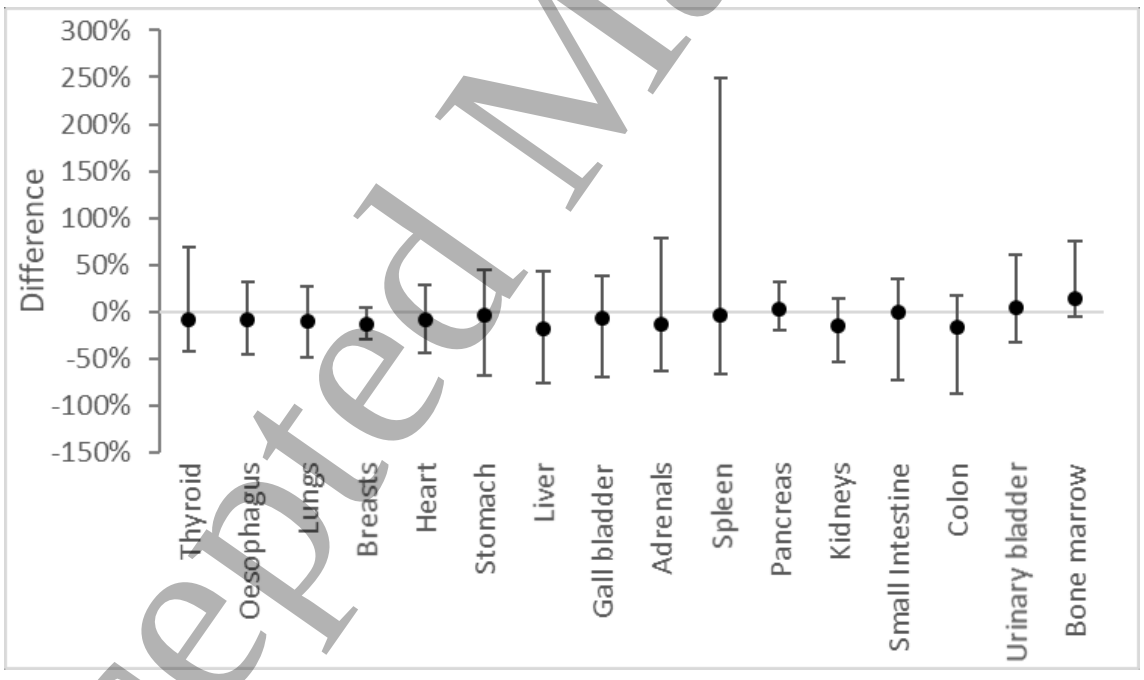

Figure 10: Mean difference (black dots) in dose for infra-renal EVAR when assuming all imaging is done in the PA projection, relative to doses estimated using individual RDSR information. A positive difference means dose estimates are higher when assuming all imaging is PA. Vertical bars represent range of differences.

Discussion:

In this study, we have estimated patient doses for a sample of endovascular aneurysm repair procedures using detailed exposure information and realistic anatomical models. Organs within the exposed region typically received absorbed doses of 50-100 mGy, though some procedures involved organ doses of several hundred mGy. Based on kerma area product, doses from EVAR are higher than most fluoroscopy procedure types, in which average P_{KA} is typically less than 50 Gy cm^2 (27). A true comparison would require the estimation of organ doses for these other procedure types, however. Mean effective doses were equivalent to perhaps 3-10 single phase abdominal CT scans. However, these high doses must be placed in the context of the high success rate of EVAR (28), the risks from open surgical aneurysm repair and the risk of catastrophic haemorrhage from untreated aneurysms. Patients undergoing EVAR are typically aged over 70 years (*e.g.* (9, 29-31)). While we must assume these patients live long enough for radiation induced cancers to develop, risks are likely to be relatively small. For many of the most heavily exposed sites, including the kidneys, small intestine and pancreas, evidence of an association with radiation exposure is limited (32). The main risks are likely to be colon cancer, leukaemia, and in the case of thoracic EVAR, lung cancer.

Average organ doses estimated using detailed exposure information from radiation dose structured reports were not grossly different from those either assuming a single beam angle (i.e. PA) or those based on average conversion factors for the whole sample of examinations. Likewise, average doses estimated using MCNP and realistic phantom models were reasonably similar to those obtained using PCXMC and stylised phantoms. This is reassuring, given that almost all previous patient dose estimates for EVAR have used PCXMC (*e.g.* (5, 9, 29-31)). Large differences were found for individual procedures, however, meaning the use of PCXMC or the $CF_{P_{KA}\rightarrow D}$ conversion factors presented in Tables 6-8 may be better suited to non-individualised purposes such as audits. Differences between dose estimates obtained using MCNP/ICRP and PCXMC/ORNL approaches may be due to (1) the lack of male/female specific phantoms in PCXMC, (2) the inability to directly model in PCXMC table attenuation and backscatter of x-rays by the table, (3) differences in organ shapes and locations, (4) different particle interaction cross section libraries, and (5) different x-ray spectra generation methods (14). The first three explanations likely dominate the observed

differences. For beams passing through the table, a reduction in intensity of ≈20% occurs. Conversely, the use of female phantoms, as opposed to male, results in an approximately 30% increase in dose (though this varied considerably between organs). Where PCXMC is used, the input P_{KA} could be reduced to account for table attenuation prior to simulation, while the phantom representing a 15-year old individual may give a better approximation of female doses than the standard adult phantom.

To our knowledge, only a single previous study has estimated organ doses from EVAR procedures. Blaszak and Juszkat (33) used the dose estimation tool CalDose_X (the only previous study to not use PCXMC-derived patient dose estimates). CalDose_X (34) is a free lookup-table based application, which uses conversion factors previously obtained from Monte Carlo simulations. The dose estimates of Blaszak and Juszkat are based on the anterior-posterior (AP) projection, while the PA projection was the dominant beam angle in our study (there were no AP exposures listed in the RDSRs). As expected, considering the difference in beam angles, estimated doses for anterior lying organs (e.g. stomach, bladder) are much lower in the current study, while doses for posterior lying organs (e.g. kidneys) are much higher.

Errors and uncertainties:

In this study, we used a lookup table approach to estimate patient doses, as opposed to performing 'live' Monte Carlo simulations for each exposure listed in RDSRs. The advantage of the lookup table approach is greatly increased computational speed. The sample of 183 examinations involved over 44,000 individual exposures. Performing MC simulations for each of these would take several months, while the lookup table approach allowed doses to be estimated within 10 minutes. The main disadvantage of this approach is lack of flexibility, with dose estimates restricted to conditions under which conversion factors were calculated.

Type-A uncertainties resulting from the finite number of particles tracked in Monte Carlo simulations were kept below 5% for all individual organs reported in this paper, and usually below 1%. Type-B uncertainties due to source geometry and energy spectra were reduced substantially through the use of radiation dose structured reports. Without utilising detailed beam angle information (assuming all

imaging was in the PA projection) we estimate organ dose uncertainties to be ±50%, based on the ranges shown in Figure 9.

We were unable to utilise some of the information from the radiation dose structured reports, including field size and beam centring point. Although a methodology for determining centring points from RDSRs has been developed (35) and implemented (24), incorporating different centring points would require calculation of new sets of lookup tables, thus requiring a lot of extra work. Furthermore, the region of interest in EVAR is less well defined than for other fluoroscopy procedures in which the above-mentioned methods (35) were developed. The results of the sensitivity analysis suggest that field size and centring point uncertainties are highly organ specific. We estimate uncertainties associated with field size and centring point to be ±10% for bone marrow, ±30% for colon and effective dose and ±50% for other organs (Figure 5).

Errors are introduced by the use of HVL to represent x-ray beam spectra. This is because the same HVL can be produced by different combinations of tube potential and filtration, while these different combinations yield different patient dose, per unit P_{KA}. At high HVLs (>7 mm Al), these errors are very small (<5 %), though may exceed 20% as the HVL is decreased below around 4 mm Al.

A further source of uncertainty is the phantom models used in Monte Carlo simulations. Although the ICRP male and female voxel phantoms are more anatomically realistic than the stylised models used in PCXMC, differences between phantom and individual patient anatomy will still introduce errors in dose estimates. Our simulations were based on adults of reference size, while in reality some are obese (11). Increased adipose tissue thickness requires increased x-ray output to maintain signal-to-noise ratio, while decreasing organ dose per unit x-ray output (36). The former effect is taken into account in the form of increased P_{KA}, while the latter is not. Consequently, organ doses for obese patients are likely to be overestimated in our study.

Differences in atomic composition of organs, blood and other fluids between real patients and phantoms will also result in errors, especially at low photon energies. The study did not incorporate the impact of iodinated contrast media (ICM), which is used in EVAR procedures to improve

visualisation of blood vessels. Previously we have shown that ICM can markedly increase absorbed dose to the endothelium of blood vessels for enhanced x-ray exposures (37) by acting as a source of secondary electrons. The lining of the aorta itself may therefore receive especially high doses from EVAR. Overall, ICM appears to result in a moderate increase in dose to organs and tissues (38), although this effect is highly dependent on iodine concentration in the main blood vessels, capillaries and interstitial tissues (37). Including the impact of iodine is extremely challenging, however, due to difficulties in determining iodine concentration in both major vessels and in the capillary network and interstitial space of organs.

Conclusion:

In this study, we have produced state-of-the-art estimates of patient doses from x-ray guided endovascular aneurysm repairs, utilising realistic anatomical models and detailed information on beam angles and x-ray energy. Patient doses from EVAR are generally high, though this is justified given the life sparing nature and high success rate of the procedure.

Acknowledgements: Thank you to David Borrego of the National Cancer Institute, Bethesda, USA, who provided the armless version of the female ICRP phantom and provided advice on source direction biasing in MCNP. This work was funded by the NIHR Health Protection Research Unit in Chemical and Radiation Threats and Hazards (no grant number), Cook Medical and the British Heart Foundation.

Conflict of interest:

All authors declare no conflict of interest.

Disclaimer: RWH, EAA and JSE are affiliated with the National Institute for Health Research Health Protection Research Unit (NIHR HPRU)) in Chemical and Radiation Threats and Hazards at Newcastle University in partnership with Public Health England (PHE). The views expressed are

those of the authors and not necessarily those of the NHS, the NIHR, the Department of Health or Public Health England.

References:

1. Adam DJ, Mohan IV, Stuart WP, Bain M, Bradbury AW. Community and hospital outcome from ruptured abdominal aortic aneurysm within the catchment area of a regional vascular surgical service. Journal of vascular surgery. 1999;30(5):922-8.
2. El-Sayed T, Patel AS, Cho JS, Kelly JA, Ludwinski FE, Saha P, et al. Radiation-Induced DNA Damage in Operators Performing Endovascular Aortic Repair. Circulation. 2017;136(25):2406-16.
3. Markar SR, Vidal-Diez A, Sounderajah V, Mackenzie H, Hanna GB, Thompson M, et al. A population-based cohort study examining the risk of abdominal cancer after endovascular abdominal aortic aneurysm repair. Journal of vascular surgery. 2019;69(6):1776-85.e2.
4. Howells P, Eaton R, Patel AS, Taylor P, Modarai B. Risk of radiation exposure during endovascular aortic repair. European journal of vascular and endovascular surgery : the official journal of the European Society for Vascular Surgery. 2012;43(4):393-7.
5. Fossaceca R, Brambilla M, Guzzardi G, Cerini P, Renghi A, Valzano S, et al. The impact of radiological equipment on patient radiation exposure during endovascular aortic aneurysm repair. European radiology. 2012;22(11):2424-31.
6. Maurel B, Sobocinski J, Perini P, Guillou M, Midulla M, Azzaoui R, et al. Evaluation of radiation during EVAR performed on a mobile C-arm. European journal of vascular and endovascular surgery : the official journal of the European Society for Vascular Surgery. 2012;43(1):16-21.
7. Hertault A, Maurel B, Sobocinski J, Martin Gonzalez T, Le Roux M, Azzaoui R, et al. Impact of hybrid rooms with image fusion on radiation exposure during endovascular aortic repair. European journal of vascular and endovascular surgery : the official journal of the European Society for Vascular Surgery. 2014;48(4):382-90.
8. Walsh C, O'Callaghan A, Moore D, O'Neill S, Madhavan P, Colgan MP, et al. Measurement and optimization of patient radiation doses in endovascular aneurysm repair. European journal of vascular and endovascular surgery : the official journal of the European Society for Vascular Surgery. 2012;43(5):534-9.
9. Thakor AS, Winterbottom A, Mercuri M, Cousins C, Gaunt ME. The radiation burden from increasingly complex endovascular aortic aneurysm repair. Insights into imaging. 2011;2(6):699-704.
10. Bannazadeh M, Altinel O, Kashyap VS, Sun Z, Clair D, Sarac TP. Patterns of procedure-specific radiation exposure in the endovascular era: impetus for further innovation. Journal of vascular surgery. 2009;49(6):1520-4.
11. Kalef-Ezra JA, Karavasilis S, Ziogas D, Dristiliaris D, Michalis LK, Matsagas M. Radiation burden of patients undergoing endovascular abdominal aortic aneurysm repair. Journal of vascular surgery. 2009;49(2):283-7; discussion 7.
12. Tapiovaara M, Siiskonen T. PCXMC: A Monte Carlo program for calculating patient doses in medical x-ray examinations. In: STUK - Radiation and Nuclear Safety Authority, editor. Helsinki, Finland2008.
13. Cristy M. Mathematical phantoms representing children of various ages for use in estimates of internal dose. US Nuclear Regulatory Commission report NUREG/CR-1159 and ORNL/NUREG/TM-367. Oak Ridge, TN: Oak Ridge National Laboratory; 1980.
14. Borrego D, Lowe EM, Kitahara CM, Lee C. Assessment of PCXMC for patients with different body size in chest and abdominal x ray examinations: a Monte Carlo simulation study. Physics in medicine and biology. 2018;63(6):065015.

15. Armstrong N, Burgers L, Deshpande S, Al M, Riemsma R, Vallabhaneni S, et al. The use of fenestrated and branched endovascular aneurysm repair for juxtarenal and thoracoabdominal aneurysms: a systematic review and cost-effectiveness analysis. Southampton (UK. Health Technol Assess. 2014;18(70):1-66.
16. Feezor RJ, Huber TS, Martin TD, Beaver TM, Hess PJ, Klodell CT, et al. Perioperative differences between endovascular repair of thoracic and abdominal aortic diseases. Journal of vascular surgery. 2007;45(1):86-9.
17. Monastiriotis S, Comito M, Labropoulos N. Radiation exposure in endovascular repair of abdominal and thoracic aortic aneurysms. Journal of vascular surgery. 2015;62(3):753-61.
18. D. B. Pelowitz e. MCNPX User's Manual, Version 2.7.0 Los Alamos National Laboratory report LA-CP-11-00438 April 2011.
19. Menzel HG, Clement C, DeLuca P. ICRP Publication 110. Realistic reference phantoms: an ICRP/ICRU joint effort. A report of adult reference computational phantoms. Annals of the ICRP. 2009;39(2):1-164.
20. International Commission on Radiation Units and Measurements (ICRU). Stopping Powers for Electrons and Positrons. ICRU Report 37. Journal of the ICRU. 1984;os19(2).
21. Cristy M. Active bone marrow distribution as a function of age in humans. Physics in medicine and biology. 1981;26(3):389-400.
22. Petoussi-Henss N, Bolch WE, Eckerman KF, Endo A, Hertel N, Hunt J, et al. ICRP Publication 116. Conversion coefficients for radiological protection quantities for external radiation exposures. Annals of the ICRP. 2010;40(2-5):1-257.
23. Poludniowski G, Landry G, DeBlois F, Evans PM, Verhaegen F. SpekCalc: a program to calculate photon spectra from tungsten anode x-ray tubes. Physics in medicine and biology. 2009;54(19):N433-8.
24. Karambatsakidou A, Omar A, Fransson A, Poludniowski G. Calculating organ and effective doses in paediatric interventional cardiac radiology based on DICOM structured reports - Is detailed examination data critical to dose estimates? Physica medica : PM : an international journal devoted to the applications of physics to medicine and biology : official journal of the Italian Association of Biomedical Physics (AIFB). 2019;57:17-24.
25. Buytaert D, Vandekerckhove K, Panzer J, Rubbens L, De Wolf D, Bacher K. Local DRLs and automated risk estimation in paediatric interventional cardiology. PloS one. 2019;14(7):e0220359.
26. International Commission on Radiological Protection (ICRP). ICRP Publication 103. The 2007 recommendations of the International Commission on Radiological Protection.; 2007.
27. Hart D, Hillier M, Shrimpton P. Doses to patients from radiographic and fluoroscopic x-ray imaging procedures in the UK - 2010 review. Chilton, Didcot: Health Protection Agency; 2012.
28. Greenhalgh RM, Brown LC, Kwong GP, Powell JT, Thompson SG. Comparison of endovascular aneurysm repair with open repair in patients with abdominal aortic aneurysm (EVAR trial 1), 30-day operative mortality results: randomised controlled trial. Lancet (London, England). 2004;364(9437):843-8.
29. Brambilla M, Cerini P, Lizio D, Vigna L, Carriero A, Fossaceca R. Cumulative radiation dose and radiation risk from medical imaging in patients subjected to endovascular aortic aneurysm repair. La Radiologia medica. 2015;120(6):563-70.
30. Geijer H, Larzon T, Popek R, Beckman KW. Radiation exposure in stent-grafting of abdominal aortic aneurysms. The British journal of radiology. 2005;78(934):906-12.
31. Weerakkody RA, Walsh SR, Cousins C, Goldstone KE, Tang TY, Gaunt ME. Radiation exposure during endovascular aneurysm repair. The British journal of surgery. 2008;95(6):699-702.
32. United Nations Scientific Committee on the Effects of Atomic Radiation (UNSCEAR). UNSCEAR 2006 Report - Effects of ionizing radiation, Annex A - Epidemiological studies of radiation and cancer. United Nations, ; 2006.
33. Blaszak MA, Juszkat R. Monte Carlo simulations for assessment of organ radiation doses and cancer risk in patients undergoing abdominal stent-graft implantation. European journal of vascular

and endovascular surgery : the official journal of the European Society for Vascular Surgery. 2014;48(1):23-8.
34. Kramer R, Khoury HJ, Vieira JW. CALDose_X-a software tool for the assessment of organ and tissue absorbed doses, effective dose and cancer risks in diagnostic radiology. Physics in medicine and biology. 2008;53(22):6437-59.
35. Omar A, Bujila R, Fransson A, Andreo P, Poludniowski G. A framework for organ dose estimation in x-ray angiography and interventional radiology based on dose-related data in DICOM structured reports. Physics in medicine and biology. 2016;61(8):3063-83.
36. Chang LA, Borrego D, Lee C. Body-weight dependent dose coefficients for adults exposed to idealised external photon fields. Journal of radiological protection : official journal of the Society for Radiological Protection. 2018;38(4):1441-53.
37. Harbron RW, Bouffler SD, Tanner R, Ainsbury EA, Pearce MS, Eakins J. The impact of iodinated contrast media on intravascular and extravascular absorbed doses in x-ray imaging: a microdosimetric analysis. Physica Medica. 2018;46:140-7.
38. Amato E, Salamone I, Naso S, Bottari A, Gaeta M, Blandino A. Can contrast media increase organ doses in CT examinations? A clinical study. AJR American journal of roentgenology. 2013;200(6):1288-93.

Appendix 1: Details of Monte Carlo methodology

Name of Monte Carlo code	MCNPX V 2.7
Cross section library	ENDF/B-VII
Source description	Photon point source. Isotropic with forward biasing. Energy spectrum in 1 keV bins.
Variance reduction	Not used
Approximate efficiency improvement techniques	Not used
Number of histories	10^7 (approx. 5-15 minutes computing time)
Step size	ESTEP set at 3 (default value)
Scored parameters	Absorbed dose in MeV/g to phantom organ cells and P_{KA} meter cell using f6 tally
Normalisation	Organ dose tally divided by P_{KA} meter tally multiplied by beam area at collimator window.

Appendix 2: Detailed description of voxel phantom models and other materials used in simulations

General characteristics:

Characteristic	Phantom	
	Male	Female
Height (cm)	176	163
Mass (kg)	73	60
Voxel volume (mm³)	36.5	15.3
Arms (Y/N)	N	N

Material composition and density:

Male phantom:

Tissue/ material	Chemical composition (%)													Density (g/cm³)
	H-1	C-6	N-7	O-8	Na-11	Mg-12	P-15	S-16	Cl-17	K-19	Ca-20	Fe-26	I-53	
Bone	3.6	15.9	4.2	44.8	0.3	0.2	9.4	0.3			21.3			1.92
Muscle	10.2	14.2	3.4	71.1	0.1		0.2	0.3	0.1	0.4				1.05
Skin	10.0	19.9	4.2	65.0	0.2		0.1	0.2	0.3	0.1				1.09
Blood	10.2	11.0	3.3	74.5	0.1		0.1	0.2	0.3	0.2		0.1		1.06
Liver	10.2	13.0	3.4	72.5	0.2		0.2	0.3	0.2	0.3				1.05
Pancreas	10.5	15.5	2.5	70.6	0.2		0.2	0.1	0.2	0.2				1.05
Brain	10.7	14.3	2.3	71.3	0.2		0.4	0.2	0.3	0.3				1.05
Heart	10.4	13.8	2.9	71.9	0.1		0.2	0.2	0.2	0.3				1.05
Eyes	9.7	18.1	5.3	66.3	0.1		0.1	0.3	0.1					1.05
Kidneys	10.3	12.4	3.1	73.1	0.2		0.2	0.2	0.2	0.2	0.1			1.05
Stomach	10.5	11.4	2.5	75.0	0.1		0.1	0.1	0.2	0.1				1.04
Small intestine	10.5	11.3	2.6	75.0	0.1		0.1	0.1	0.2	0.1				1.04
Large intestine	10.5	11.3	2.6	75.0	0.1		0.1	0.1	0.2	0.1				1.04
Spleen	10.2	11.1	3.3	74.3	0.1		0.2	0.2	0.3	0.2		0.1		1.04
Thyroid	10.4	11.7	2.6	74.5	0.2		0.1	0.1	0.2	0.1			0.1	1.04
Bladder	10.5	9.6	2.6	76.1	0.2		0.2	0.2	0.3	0.3				1.04
Testes	10.6	10.0	2.1	76.4	0.2		0.1	0.2	0.2	0.2				1.04
Adrenals	10.4	22.1	2.8	63.7	0.1		0.2	0.3	0.2	0.2				1.03
Oesophagus	10.4	21.3	2.9	64.4	0.1		0.2	0.3	0.2	0.2				1.03
Gall bladder	10.4	23.1	2.8	62.7	0.1		0.2	0.3	0.2	0.2				1.03
Prostate	10.4	23.1	2.8	62.7	0.1		0.2	0.3	0.2	0.2				1.03
Lymph	10.8	4.2	1.1	83.1	0.3			0.1	0.4					1.03
Breast	11.2	51.6	1.1	35.8	0.1			0.1	0.1					1.02
Adipose	11.4	58.8	0.8	28.7	0.1			0.1	0.1					0.95
Lungs	10.3	10.7	3.2	74.6	0.2		0.2	0.3	0.3	0.2				0.42
GI tract contents	10.0	22.2	2.2	64.4	0.1		0.2	0.3	0.1	0.4	0.1			1.04
Urine	10.7	0.3	1.0	87.3	0.4		0.1			0.2				1.04

% of all other elements is zero.

Female phantom:

Tissue/ material	Chemical element													Density (g/cm³)
	H-1	C-6	N-7	O-8	Na-11	Mg-12	P-15	S-16	Cl-17	K-19	Ca-20	Fe-26	I-53	
Bone	3.6	15.9	4.2	44.8	0.3	0.2	9.4	0.3			21.3			1.92
Muscle	10.2	14.2	3.4	71.1	0.1		0.2	0.3	0.1	0.4				1.05
Skin	10.0	19.9	4.2	65.0	0.2		0.1	0.2	0.3	0.1				1.09
Blood	10.2	11.0	3.3	74.5	0.1		0.1	0.2	0.3	0.2		0.1		1.06
Liver	10.2	13.1	3.1	72.4	0.2		0.2	0.3	0.2	0.3				1.05
Pancreas	10.5	15.7	2.4	70.5	0.2		0.2	0.1	0.2	0.2				1.05
Brain	10.7	14.4	2.2	71.3	0.2		0.4	0.2	0.3	0.3				1.05
Heart	10.4	13.8	2.9	71.9	0.1		0.2	0.2	0.2	0.3				1.05
Eyes	9.7	18.3	5.4	66.0	0.1		0.1	0.3	0.1					1.05
Kidneys	10.3	12.5	3.1	73.0	0.2		0.2	0.2	0.2	0.2	0.1			1.05
Stomach	10.5	11.4	2.5	75.0	0.1		0.1	0.1	0.2	0.1				1.04
Small intestine	10.5	11.4	2.5	75.0	0.1		0.1	0.1	0.2	0.1				1.04
Large intestine	10.5	11.4	2.5	75.0	0.1		0.1	0.1	0.2	0.1				1.04
Spleen	10.3	11.2	3.2	74.3	0.1		0.2	0.2	0.2	0.3				1.04
Thyroid	10.4	11.8	2.5	74.5	0.2		0.1	0.1	0.2	0.1			0.1	1.04
Bladder	10.5	9.6	2.6	76.1	0.2		0.2	0.2	0.3	0.3				1.04
Ovaries	10.5	9.4	2.5	76.6	0.2		0.2	0.2	0.2	0.2				1.04
Adrenals	10.4	22.8	2.8	63.0	0.1		0.2	0.3	0.2	0.2				1.03
Oesophagus	10.4	22.2	2.8	63.6	0.1		0.2	0.3	0.2	0.2				1.03
Gall bladder	10.5	23.5	2.8	62.2	0.1		0.2	0.3	0.2	0.2				1.03
Uterus	10.5	28.6	2.5	57.6	0.1		0.2	0.3	0.1	0.2				1.03
Lymph	10.8	4.2	1.1	83.1	0.3			0.1	0.4					1.03
Breast	11.2	51.6	1.1	35.8	0.1			0.1	0.1					1.02
Adipose	11.4	58.9	0.7	28.7	0.1			0.1	0.1					0.95
Lungs	10.3	10.7	3.2	74.6	0.2		0.2	0.3	0.3	0.2				0.42
GI tract contents	10.0	22.2	2.2	64.4	0.1		0.2	0.3	0.1	0.4	0.1			1.04
Urine	10.7	0.3	1.0	87.3	0.4		0.1			0.2				1.04

Other materials:

Tissue/ material	Chemical element													Density (g/cm³)
	H-1	C-6	N-7	O-8	Na-11	Mg-12	P-15	S-16	Cl-17	K-19	Ca-20	Fe-26	I-53	
Air			80.0	20.0										0.0013
Bed		100.0												1.40

Coronal plane images of male (left) and female (right) phantoms at the level of the kidneys (male/female images are not to same scale)